

Modelling vibro-acoustic coupling in flexible micro-perforated plates by a patch-impedance approach

Muttalip Aşkın Temiz^{a,*}, Jonathan Tournadre^b, Ines Lopez Arteaga^{a,c}, Avraham Hirschberg^d

^aEindhoven University of Technology, Department of Mechanical Engineering, The Netherlands

^bKU Leuven, Department of Mechanical Engineering, Celestijnenlaan 300, B. 3001 Leuven, Belgium

^cKTH Royal Institute of Technology, Department of Aeronautical and Vehicle Engineering, Stockholm, Sweden

^dEindhoven University of Technology, Department of Applied Physics, The Netherlands

ARTICLE INFO

Article history:

Received 3 November 2016

Received in revised form 27 February 2017

Accepted 13 April 2017

Available online 25 April 2017

2010 MSC:

70-80

74F10

Keywords:

Flexible micro-perforated plates

Vibro-acoustic coupling

Acoustic transfer impedance

Absorption coefficient

Finite element method

ABSTRACT

This study proposes a Finite Element (FE)-based efficient numerical model of the vibro-acoustic coupling in flexible micro-perforated plates (f-MPPs) where each perforation is described as an imposed impedance boundary condition (uniform impedance patch) on the plate. This approach opens the possibility of predicting the influence of perforation distribution on the acoustic performance of f-MPP. Micro perforated plates have been a topic of interest as a promising sound absorber in a wide range of applications, from room acoustics to combustion systems. One great advantage of these plates is that it gives the designer the freedom of choice on material in production. Depending on the material and the dimensions, the acoustical modes of the medium can couple with the structural modes of the plate. This coupling changes the number of absorption peaks, frequency and amplitude of the Helmholtz resonance of the system, therefore the coupling becomes an extra parameter in the design process. Current analytical models superpose the mechanical impedance of the plate with the acoustic impedance of the perforations to compute this coupling. This approach works fairly well for plates with uniform perforation distribution. This study proposes a numerical method which assumes perforations as discrete impedance patches on the flexible plate so that they can be considered separately. The method couples the solution of the Helmholtz equation in air with shell plate theory to model the vibro-acoustic effects and the impedance patches are represented as imposed transfer impedance boundary conditions. The assessment of the method is performed in terms of comparing the calculated absorption coefficient values from the simulations of several test cases, fundamental theories and measurement results from the literature. The simulation results agree both with these theoretical limits and measurement results. The use of the method is illustrated by considering an example of the influence of modification of the spatial distribution of perforations on the sound absorption of a membrane.

1. Introduction

Micro-perforated plates (MPPs) have been designated as high potential sound absorbers by Maa [1] for various applications including the ones with severe environments. Before the study of Maa [1], they were used only as protective layer for classical sound absorbers. MPPs are plates with small perforations whose diameter is in the order of 10^{-1} mm with low porosity values, i.e. $\phi = \mathcal{O}(1\%)$. When backed by a cavity, they provide broadband acoustic dissipation.

The present study is limited to the amplitude range for which the behaviour can be described by a linear model. This excludes damping due to vortex shedding. The linear sound absorption mechanism in MPPs is based on the conversion of the kinetic energy of the fluid particles into heat energy due to the viscous resistance in the perforations. As the viscous resistance increases with the relative velocity between the plate and the fluid, the kinetic energy loss of the particles and the corresponding sound absorption is larger when the excitation frequency approaches to the Helmholtz resonance frequency of the back cavity. For a rigid MPP, the relative particle velocity of the air is the same for each perforation at all frequencies when excited by a planar acoustic wave. On the other hand, when the plate is flexible, at certain frequencies the plate vibrates with the mode shape depending on its

* Corresponding author.

E-mail address: m.a.temiz@tue.nl (M.A. Temiz).

This is a pre-print version.

Published in Applied Acoustics (2017), Vol. 125, pp. 80-90.

DOI: 10.1016/j.apacoust.2017.04.012

geometry, excitation frequency, boundary conditions and material. Due to this mode shape, even under acoustic plane wave excitation, the relative air particle velocity with respect to the plate depends on the position of the perforation within the plate. Therefore, the perforation position is potentially a design parameter in flexible micro-perforated plates (f-MPPs).

Sound absorption by flexible plates is a known phenomenon in room acoustics. One of the first analytical models for a flexible plate, which does not have perforations but backed by an air cavity, is provided by Cremer and Müller [2]. In this model, they couple the bending waves of the flexible plate with the acoustic waves of the air cavity. An important contribution to this model is made by Basten et al. [3]. They consider an enclosed air cavity between two flexible plates and the distance between these plates are small. Basten et al. [3] analytically show that, such a small gap between the flexible plates causes the visco-thermal effects to become dominant in the cavity.

On the MPP side, the first scientists to observe that plate vibrations affect the absorption mechanism are Lee and Swenson [4]. In their experiments, they report an additional absorption peak which cannot be modelled by the rigid MPP theory. The first analytical model including the flexible effects in MPPs is given by Lee et al. [5]. Inspired by their work, Toyoda et al. [6] propose a similar approach for modelling of f-MPPs having circular geometry. Both Lee et al. [5] and Toyoda et al. [6] calculate the structural impedance of the flexible plate using modal analysis and combine it with the acoustic transfer impedance defined by Maa [1]. In both of these studies, the mathematical models are verified by experiments. Bravo et al. [7,8] consider a case where the back cavity walls are flexible and provide a theoretical model where the absorption mechanism is governed by the relative velocity between the air particles and the flexible plate. They verify this model by experiments. Li et al. [9] propose a sophisticated model to account for the non-zero velocity boundary condition at the inner walls of the perforations. This boundary condition redefines the classical acoustic transfer impedance expression by Maa [1].

Besides the analytical and empirical approaches described so far, some numerical models employing finite element method (FEM) have been proposed. Hou and Bolton [10] model the plate as a porous material and they include the vibrations effects through the elastic frame model. They focus on the effect of plate profile (such as bent and curved plates) on the absorption coefficient. Wang and Huang [11] investigate the effect of complex back-cavity shapes in acoustic response of f-MPPs. They couple the structural vibrations of the plate with the acoustics of the perforations and the back cavity. In their model, air particle velocity in the perforations are averaged over the flexible plate. Okuzono and Sakagami [12] propose a numerical model to analyse the sound field in room acoustics which is computationally low-cost. However, they assume the plate as an additional mass vibrating in front of the back cavity thus it does not consider the structural plate modes. Moreover, as previous studies, they average the acoustic transfer impedance of the perforations over the plate. On the other hand, Carbajo et al. [13] consider each perforation separately in their FE model. They represent the entire acoustic domain (including the perforations) with linearized Navier-Stokes equations to be able to capture the visco-thermal effects. They study the interaction between the perforations. Even though they do not take plate flexibility into account, they report that their model is computationally demanding.

The FE model proposed in the current study makes it possible to model (i) the vibro-acoustic coupling in f-MPPs, (ii) viscous losses in the small perforations, and (iii) the effect of perforation distribution. This is achieved by coupling the Helmholtz equation [14] and Kirchhoff's thin plate equation [15] in the numerical domain, while each perforation is represented by transfer impedance boundary

patches on the flexible plate separately. The boundary condition for these patches take the viscous losses into account. Considering this feature, the model presented in this study is more efficient than the ones using linearized Navier-Stokes equations [13] to capture the viscous effects of the micro-perforations.

To validate the theory, a cylindrical impedance tube is modelled numerically and the acoustic properties of the f-MPP with a back cavity is assessed in terms of absorption coefficient, α_A . The model outputs are compared with fundamental plate and acoustic theories and experiments reported in the literature. The use of the method is illustrated by considering an example of the influence of modification of the spatial distribution of perforations on the sound absorption of a thin plate.

2. Theoretical background

The numerical domain of the impedance tube configuration is presented schematically in Fig. 1.

The numerical model is composed of two domains: a structural domain (shell) and an acoustic domain. This section provides the governing equations used for modelling these domains.

2.1. Structural domain

The equation of motion of the thin, homogeneous flexible plate shown in Fig. 1 is given by Kirchhoff [15] as

$$D_p \nabla^2 \nabla^2 w(r) - \rho_p t_p \omega^2 w(r) = \hat{P}, \quad (1)$$

where ∇^2 is the Laplacian operator, $w(x, y)$ is the plate displacement in the z -direction, ρ_p is the plate density (mass per unit of surface), t_p is the plate thickness; \hat{P} is the external pressure difference acting on the plate; $D_p = E(1 + j\eta)t_p^3/[12(1 - \nu^2)]$ is the flexural rigidity of the plate where j is the imaginary number ($j^2 = -1$), E is the Young's modulus, η is the loss factor and ν is the Poisson ratio of the plate material. As the typical porosity of an f-MPP is in the order of 10^{-2} [16], the effect of perforations on the structural properties of the flexible plate is ignored for the modelling.

2.2. Acoustic domain

Domains ① and ② in Fig. 1 are acoustic domains and they are assumed to be excited by harmonic plane waves. Furthermore, thermo-viscous losses at the sound-hard boundaries are negligible in these acoustic domains. Under these assumptions, the spatial pressure distribution in frequency domain is given by Helmholtz equation [14]

$$\omega^2 \hat{p}_n(z) + c_0^2 \nabla^2 \hat{p}_n(z) = 0, \quad (2)$$

where $\omega = 2\pi f$ is the radial frequency, c_0 is the speed of sound in air and \hat{p}_n is the acoustic pressure in frequency domain for acoustic medium n ; i.e. $n = 1$ for the impedance tube and $n = 2$ for the back cavity domains, respectively (see Fig. 1).

The two acoustical domains in Fig. 1 are connected through micro-perforations which can be considered as independent *uniform impedance patches* on the flexible plate. These patches are defined as imposed transfer impedance boundaries in the numerical model and the mathematical expression for each patch is given by Temiz et al. [16] as

$$Z_t = \frac{\hat{p}_1 - \hat{p}_2}{\hat{u}_p} = j\omega t_p \rho_0 \left[1 - \frac{2}{Sh\sqrt{-j}} \frac{J_1(Sh\sqrt{-j})}{J_0(Sh\sqrt{-j})} \right]^{-1} + 2\alpha_s R_s + j\delta_s \omega \rho_0 \frac{d_p}{2}, \quad (3)$$

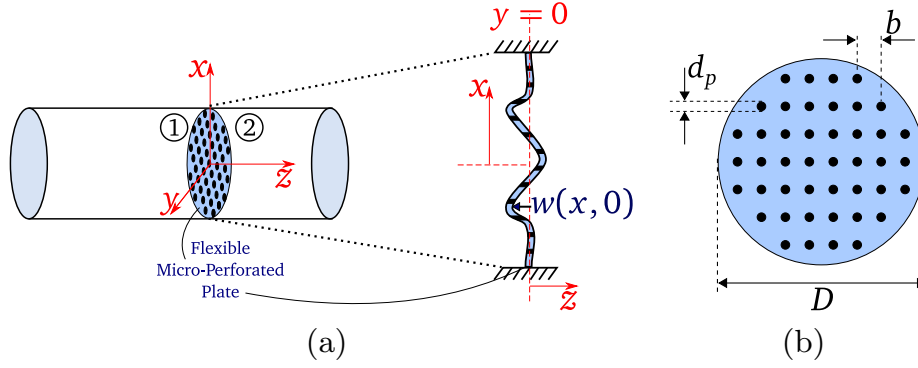


Fig. 1. (a) The schematic drawing of the flexible micro-perforated plate (f-MPP) placed between the impedance tube (Domain ①) and the back cavity (Domain ②). The plate displacement vector $w(x, y)$ is also illustrated on the cross-sectional view of the f-MPP; (b) front view of an f-MPP whose perforations are distributed uniformly.

where \hat{u}_p is the average acoustic particle velocity in the perforation, ρ_0 is the density of the acoustic medium and J_m is the Bessel function of first kind of order m . The other parameters in Eq. (3) are calculated for square-edged perforations as [16]

$$Sh = d_p \sqrt{\omega \rho_0 / (4\mu)}, \quad (4a)$$

$$R_s = 0.5 \sqrt{2\mu \rho_0 \omega}, \quad (4b)$$

$$\alpha_s = 5.08 Sh^{-1.45} + 1.70, \quad (4c)$$

$$\delta_s = 0.97 \exp(-0.20 Sh) + 1.54, \quad (4d)$$

where Sh is the Shear number: the ratio of the perforation diameter to the oscillating boundary layer thickness, μ is the dynamic viscosity of air (1.82×10^{-5} kg/ms at 20 °C), R_s is the surface resistance, α_s and δ_s are resistive and reactive end-correction coefficients for circular orifices with square-edge geometries. Note that as δ_s is a function of Sh , it takes into account the effect of viscosity on the inertance. Other expressions for other edge geometries are proposed by Temiz et al. [16]. The expression given in Eq. (3) is valid when the perforations are far enough from each other, so that they do not interact. Eq. (4) is based on numerical simulations and was validated experimentally [16].

3. Numerical model

The numerical model is built in the finite element program COMSOL Multiphysics® (ver. 5.0) [17] using the built-in *Pressure Acoustics* and *Plate* modules. The model represents a cylindrical impedance tube set-up with two microphones to estimate the absorption coefficient. At one end of the tube, the flexible micro-perforated plate and the back cavity is placed where the other end is used for introducing the acoustic plane wave into the system. The micro-perforations are modelled as described in the previous section. The simplified representation of the numerical domain, which describes the boundary conditions employed, is given in Fig. 2.

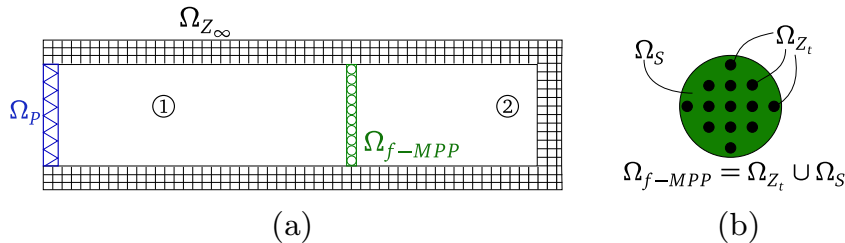


Fig. 2. The description of the boundary conditions used for modelling the (a) impedance tube; (b) f-MPP: Ω_p is the imposed pressure, Ω_{∞} is the sound-hard, Ω_{f-MPP} is the f-MPP, Ω_{z_t} is the imposed transfer impedance and Ω_s is the vibro-acoustic coupling boundary.

3.1. Boundary conditions

Four types of boundary conditions are used to model the configuration represented in Fig. 1.

- Imposed pressure boundary (Ω_p): To represent the plane wave excitation incident to the f-MPP, this boundary condition is employed at the upstream of the tube geometry. The equation for this boundary is

$$\hat{p}|_{\Omega_p} = \hat{p}_{ex}, \quad (5)$$

where \hat{p}_{ex} is the prescribed pressure amplitude (in frequency domain).

- Sound-hard boundary (Ω_{∞}): The normal acoustic velocity vanishes at the side walls of the impedance tube and the termination of the back cavity by this boundary condition.

$$\hat{u}|_{\Omega_{\infty}} = 0. \quad (6)$$

- Imposed transfer impedance boundary (Ω_{z_t}): The change ($\hat{p}_1 - \hat{p}_2$) in the acoustic pressure from Domain ① to ② through the perforations is related to the particle velocity (\hat{u}_p) by the boundary condition, on the patch surface

$$\frac{\hat{p}_1 - \hat{p}_2}{\hat{u}_p}|_{\Omega_{z_t}} = Z_t, \quad (7)$$

where Z_t is calculated by using Eq. (3).

- Vibro-acoustic coupling boundary (Ω_s): On this boundary, the acoustics of Domains ① and ② are coupled with the structural vibrations of the shell domain. This is achieved by the following equations

$$\hat{u}(x, y)|_{\Omega_s} = \frac{dw(x, y)}{dt} = j\omega w(x, y) \quad (8a)$$

$$\hat{p}|_{\Omega_s} = \hat{p}_1|_{\Omega_s} - \hat{p}_2|_{\Omega_s}, \quad (8b)$$

where Eq. (8a) couples the plate displacements with the acoustic particle velocity and Eq. (8b) couples the forcing source term in Eq. (1) on the flexible plate with the acoustic pressure difference between Domains ① and ②.

The boundary condition represented as Ω_{f-MPP} is the combination of Ω_{z_i} and Ω_s , as can be seen in Fig. 2.

3.2. Finite element model

The finite element model of the configuration is obtained by discretizing Eqs. (1) and (2) over the numerical domain using quadratic shape function for both acoustic and structural domains. After introducing the boundary conditions (Eqs. (5)–(8)) into the weak form of the governing equations (Eqs. (1) and (2)), the system of equations representing the numerical model takes the following form:

$$\left\{ \begin{bmatrix} \mathbf{K}_s & \mathbf{K}_c \\ 0 & \mathbf{K}_a \end{bmatrix} + j\omega \begin{bmatrix} \mathbf{C}_s & 0 \\ 0 & \mathbf{C}_a \end{bmatrix} - \omega^2 \begin{bmatrix} \mathbf{M}_s & 0 \\ \mathbf{M}_c & \mathbf{M}_a \end{bmatrix} \right\} \begin{Bmatrix} \mathbf{w}_u \\ \mathbf{p}_u \end{Bmatrix} = \begin{Bmatrix} \mathbf{F}_{si} \\ \mathbf{F}_{ai} \end{Bmatrix}, \quad (9)$$

where, \mathbf{K} is the stiffness, \mathbf{M} is the mass, \mathbf{C} is the dissipation and \mathbf{F} is the forcing matrices. The subscripts ‘a’, ‘s’ and ‘c’ represent the words *acoustic*, *structural* and *coupling*. The vectors \mathbf{w}_u and \mathbf{p}_u stand for the free plate displacement and acoustic pressure vectors, respectively. These are the vectors that are not imposed as boundary conditions and need to be solved for. The imposed boundary conditions introduced in the acoustic and structural forcing vectors, \mathbf{F}_{ai} and \mathbf{F}_{si} . Finally, Eqs. (8a) and (8b) are represented by \mathbf{M}_c and \mathbf{K}_c , respectively [18].

The system of equations given in Eq. (9) is solved by using a direct linear solver. For a model containing $\sim 360,000$ elements and $\sim 750,000$ degrees of freedom, the simulation time for a single frequency is ~ 210 s on a workstation with the following specifications: 4-core 2.60 GHz processor and 16 GB RAM.

3.3. Estimation of the absorption coefficient

In this study, the absorption coefficient is represented by *beta* in order not to confuse it with the resistive end-correction coefficient α . To calculate the absorption coefficient α_A , the two-microphone method by Bodén and Åbom [19] is applied to the numerical model. Two microphone positions, z_{m1} and z_{m2} are chosen on Domain ① and the pressure values are averaged by section at these two positions in z as \hat{p}_{m1} and \hat{p}_{m2} . Using these pressure readings, wave decomposition is performed to obtain complex amplitudes of the right and left travelling pressure waves, \hat{p}^+ and \hat{p}^- respectively. Therefore, the absorption coefficient is calculated as

$$\alpha_A = 1 - \left| \frac{\hat{p}^-}{\hat{p}^+} \right|^2. \quad (10)$$

3.4. Compensation for inviscid reactance

Since the numerical method described in this section allows one to model the perforations separately, it is referred here as the *discrete model*. On the contrary, the conventional analytical model assumes an average transfer impedance value over the plate and lumps this value to the MPP to compute the acoustic properties of the system, therefore it is referred to as the *lumped model* in the present paper. Provided that the perforations are far enough from each other, so that no interactions between perforations take place, the discrete and lumped models should provide comparable results for the rigid plate. Please note that, for the rigid plate mod-

Table 1

Properties of the cases from Toyoda et al. [6] used for comparing the discrete and lumped models. Please see Fig. 3 for the definition of parameters.

	Case A1	Case A2	Case A3
d_p [mm]	0.5	1.0	2.0
t_p [mm]	0.5	0.5	0.5
b [mm]	10	10	10
n_p	76	76	76
ϕ [%]	0.2	0.8	3.1
D [mm]	100	100	100
L [mm]	300	300	300
L_c [mm]	50	50	50

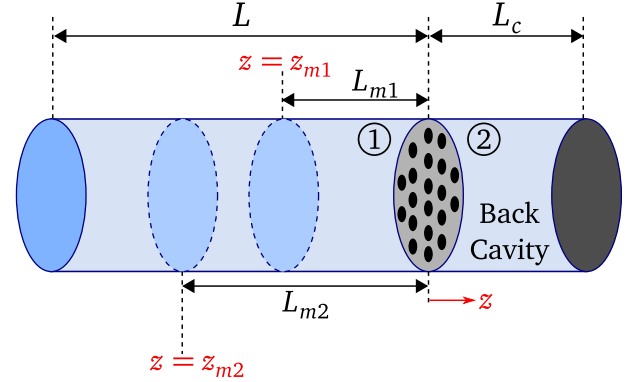


Fig. 3. Geometric parameters of the numerical domain.

elling, the vibro-acoustic boundary condition (Ω_s) is replaced with the sound-hard boundary condition (Ω_{z_n}).

To verify this, three test cases are considered. The physical properties of these cases are provided in Table 1 and Fig. 3.

In Table 1, b is the distance between the two neighbouring perforations, n_p is the number of perforations on the plate, L is the length of the impedance tube and L_c is the depth of the back cavity (see Fig. 3). These parameters are taken from the study by Toyoda et al. [6].

The comparison between the absorption coefficients predicted by the lumped and discrete models for Cases A1 to A3 is given in Fig. 4. As it can be seen in these graphs, the discrepancy between the analytical results and the numerical ones increase from Cases A1 to A3. Considering the parameters given in Table 1, only perforation diameter and plate porosity values differ among the test cases.

The same discrepancy is reported by Temiz et al. [18] with another FE program, namely LMS Virtual.Lab [20]. Hence, the discrepancy between the predictions of the lumped and discrete models is not solver dependent.

Keeping in mind that the Helmholtz equation does not take the viscous effects into account, the frequency shift observed in Fig. 4 is a result of reactance only. In fact, Eq. (3) takes a reactance (end-correction δ_s) into account describing the inertia of the non-uniform acoustic flow around the opening of the perforations. The solution of the Helmholtz equation should therefore disregard this effect. To eliminate this inviscid reactance contribution (δ_H) by the Helmholtz equation, its value is estimated and subtracted from Eq. (3). This subtraction can be performed under the assumptions that the acoustic flow is almost incompressible around the perforations and that acoustic impedance can be superposed due to the linearity of the system.

This new expression is referred as the *modified transfer impedance* and should be used at the imposed transfer impedance boundaries in the proposed numerical model. To calculate the

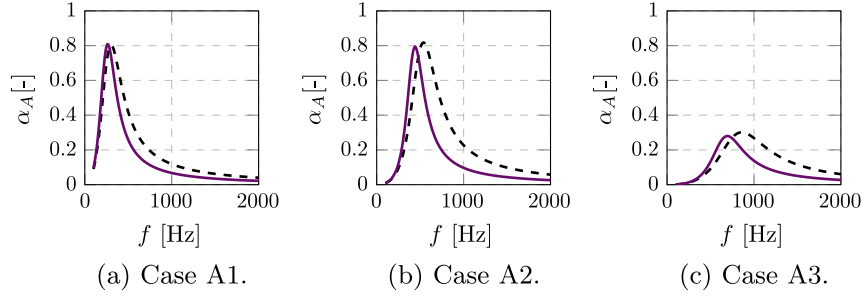


Fig. 4. Comparison of the absorption coefficients calculated with the discrete model (—) and the conventional lumped model (---).

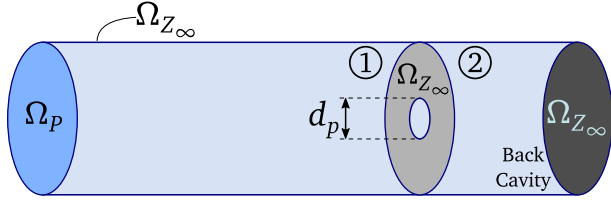


Fig. 5. Schematic representation of the numerical geometry used in the parametric study for calculating the inviscid reactance contribution of an orifice.

inviscid reactance contribution, a set of simulations have been carried out. The numerical domain for this set of simulations is almost identical to the one described so far in this paper. The schematic description of the numerical domain used in this parametric study is given in Fig. 5 and the parameters investigated are provided in Table 2. By examining Fig. 5, the differences can be noted: a single orifice is modelled (instead of an MPP) and the plate is modelled as a rigid boundary. Since it is a basic acoustic model, the meshing is performed by the built-in meshing tool by COMSOL. The mesh size is selected as the *Extremely Fine* level, which provides the finest grid in the numerical domain. Using the results from this numerical model, a parametric study is performed. The results are represented in terms on non-dimensional parameters so that they can be generalized.

The single orifice illustrated in Fig. 5 is modelled with the Acoustic module of COMSOL Multiphysics in frequency domain. Therefore no viscous effects are taken into consideration. As a result, the acoustic reactance of the orifice in Fig. 5, $\Im\{Z_t\}_H$, is the inviscid reactance contribution. Please note that subscript *H* represents the word *Helmholtz* and indicates the inviscid contribution. This parameter is non-dimensionalized by normalizing it as proposed by Ingard [21]

$$\delta_H = \frac{2\Im\{Z_t\}_H}{\rho_0 \omega d_p}. \quad (11)$$

From Table 2, simulations are run for $7 \times 4 \times 3 = 84$ different parameter combinations. Among these combinations, the effect of frequency change between the same porosity and perforation

Table 2
The parameters used in simulations to calculate the inviscid reactance contribution from the Helmholtz equation.

Porosity (ϕ) [%]	Perforation diameter (d_p) [mm]	Frequency (f) [Hz]
0.1	0.5	200
0.2	1.0	1000
0.4	2.0	2000
0.8	4.0	
1.6		
3.2		
5.0		

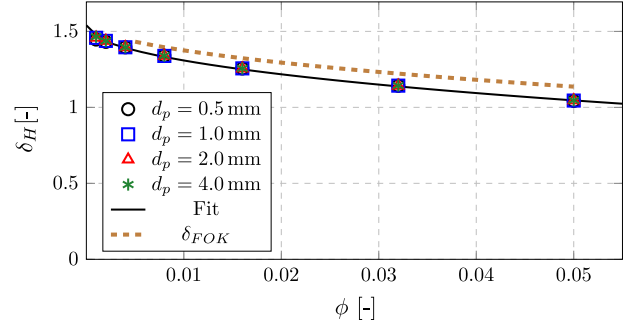


Fig. 6. The change of inviscid reactive end-correction coefficient with respect to the porosity. For $0.5 \text{ mm} \leq d_p \leq 4.0 \text{ mm}$, the perforation diameter has negligible effect on δ_H .

diameter values are found to be less than 1% for δ_H , therefore the number of points to be investigated is reduced to 28 by taking an average value of the three frequency values of the same combination. The resulting 28 data points are plotted with respect to porosity in Fig. 6.

It is evident from Fig. 6 that the inviscid reactive end-correction δ_H only depends on the porosity. Even for various diameter values from 0.5 mm to 5.0 mm, the same δ_H value is found for the same porosity. Hence, to estimate the non-dimensional inviscid reactance, a fit which is a function of porosity only is proposed such as

$$\delta_H = 0.85\phi - 2.40\sqrt{\phi} + 1.54, \quad 0 \leq \phi \leq 1. \quad (12)$$

The quality of the fit given in Eq. (12) is $r^2 = 0.9998$, where $(1 - r^2)$ is the variance of the fit.

The fit is calculated in such a way that when the porosity is unity, in other words when the orifice size is equal to the duct diameter, $\delta_H = 0$ is satisfied. On the other hand, when the porosity becomes very small, the fit value approaches to 1.54. This value is comparable to the theoretical limit value calculated by Pierce [22] who obtains the analytical value for the low frequency limit of the length of the oscillating fluid mass at a circular orifice in an infinite (thin) baffle plate as $\pi/2 = 1.57$ times the orifice radius. Therefore in the very low porosity limit, the fit proposed in Eq. (12) leads to an error of no more than 2% compared to the theoretical limit of Pierce [22].

Moreover, Tayong et al. [23] discuss the hole interaction effect on the acoustic reactance with the help of Fok's function which also depends on porosity. Their correction is compared to the fit given in Eq. (12) for $0.005 \leq \phi \leq 0.05$ and a very similar trend is observed between the two calculations (see Fig. 6). Therefore, we conclude that using the expression given in Eq. (12) for compensating the excess reactance should be adequate.

Finally, the modified transfer impedance Z_t^* , which is used in the imposed transfer impedance boundary layer in the discrete numerical model, is updated as

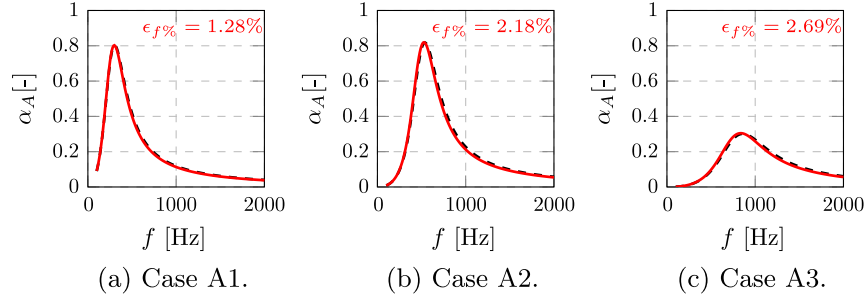


Fig. 7. Comparison of the absorption coefficients calculated with the discrete model using the modified transfer impedance (—) and the conventional lumped model (---).

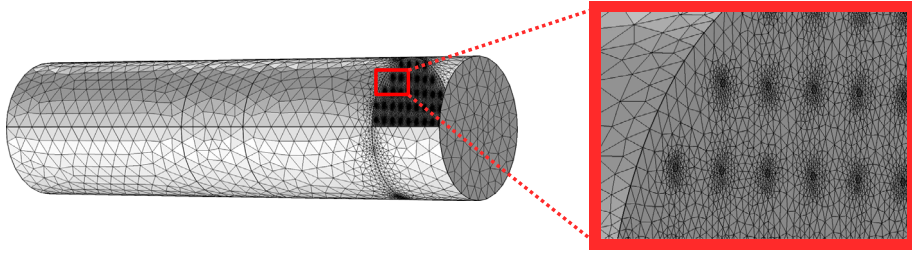


Fig. 8. The example of typical meshing of the numerical geometry. The meshing is performed with COMSOL's built-in physics controlled meshing tool and some part of the side surface is left open to show the meshing around the perforations.

$$Z_t^* = j\omega t_p \rho_0 \left[1 - \frac{2}{Sh\sqrt{-j}} \frac{J_1(Sh\sqrt{-j})}{J_0(Sh\sqrt{-j})} \right]^{-1} + 2\alpha_s R_s + j(\delta_s - \delta_H)\omega\rho_0 \frac{d_p}{2}. \quad (13)$$

please recall that α_s and δ_s are resistive and reactive end-correction coefficients for a circular perforation with square-edge profile and their value can be calculated by Eq. (4).

In Fig. 7, the comparison between the predicted absorption coefficient for the conventional analytical model and the discrete model which uses the modified transfer impedance is made. For each Case, the relative percentage error is calculated as

$$\epsilon_{f\%} = \frac{|f_{peak-lm} - f_{peak-dm}|}{f_{peak,m}} 100\%, \quad (14)$$

where f_{peak} is the frequency where the absorption peak is observed, subscripts lm and dm represent the lumped and discrete models respectively. The calculated relative percentage errors are presented in Fig. 7, also.

It can be seen that the discrepancy between the two prediction is practically eliminated when the modified transfer impedance proposed in Eq. (13) is applied in the discrete model.

3.5. Meshing

The mesh used for discretizing the numerical domain is built by COMSOL automatically based on the physics used in the model. The *extra-fine* mesh option is chosen for all models in this study. Although it is built automatically, the mesh is manually checked to satisfy following conditions: (1) the largest acoustic element is never larger than 1/10 of the smallest acoustic wave length of interest; (2) there are at least 8 elements for each perforation; (3) the mesh around the perforation is finer than the rest of the acoustic domain matching locally the perforation mesh.

In the model, triangular elements are used for surfaces and boundaries whereas tetrahedral elements are used for volumes.

Both the acoustic and shell domains are meshed with quadratic elements. An example of the meshed geometry is shown in Fig. 8. The study for mesh convergence is discussed in A.

4. Validation of the discrete numerical model and discussions

The validation of the discrete numerical model is partly performed in the previous chapter by the parametric study for evaluating the contribution of the inviscid reactance. Fig. 7 provides the comparison between the discrete and lumped models of the acoustic absorption of an MPP backed by a cavity for rigid plates. In this section, the predicted absorption coefficients for two rigid plate configurations are compared to measured absorption coefficients and then the effect of vibro-acoustically coupled system is discussed by comparing results from both fundamental analytical models and measurements by Toyoda et al. [6] with the discrete numerical model.

4.1. Rigid plate

The impedance tube used for the experimental validation of the discrete numerical model is the same set-up described in the study

Table 3

Properties of the samples used in the experimental validation of the discrete numerical model for the rigid plate case. The measurements are carried out with the impedance tube set-up described by Temiz et al. [16].

	Case A4	Case A5
d_p [mm]	0.8	1.6
t_p [mm]	1.0	1.6
b [mm]	8	15
n_p	29	7
ϕ [%]	0.7	0.7
D [mm]	50	50
L [mm]	150	150
L_c [mm]	20	20
Material	Brass	Brass

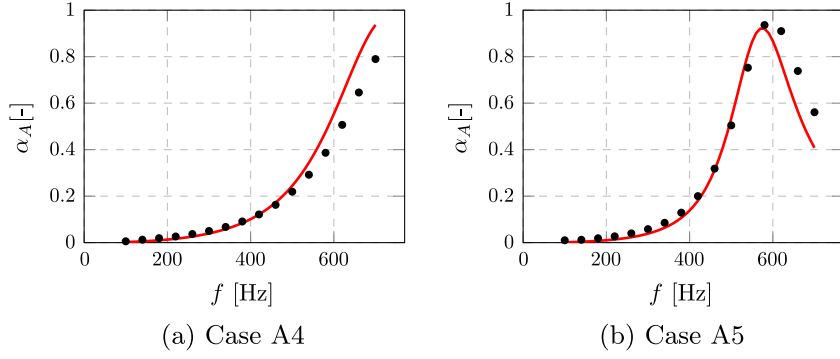


Fig. 9. Comparison between the (original) experiments (•) and numerical model (—) with modified transfer impedance in Eq. (13).

by Temiz et al. [16]. The physical properties of the samples used in this validation is provided in Table 3.

The measurements are performed in the frequency interval of $100 \text{ Hz} \leq f \leq 700 \text{ Hz}$. The experimental and numerical results are plotted together in Fig. 9. As it can be seen from the plots, the numerical model successfully captures the general absorption behaviour of the rigid MPPs.

The samples defined in Cases A4 and A5 have already been used in an earlier study by Temiz et al. [24] and they are reported to have some uncertainties in the perforation geometry. The perforations on these samples are manufactured by drilling and some of them have more triangular shape than circular. The reason for the frequency shift between the discrete numerical model and the measurements in Fig. 9 can be this uncertainty.

4.2. Flexible plate

To validate the discrete numerical model in terms of vibro-acoustic coupling, the test cases from Toyoda et al. [6] are used and their properties are provided in Table 4. To include the structural effects into the model, the f-MPP boundary condition is applied on the plate (See Fig. 2 and Eq. (8)).

Although the test cases are clearly defined in the study by Toyoda et al. [6], the density of the flexible plate is not explicitly provided. Instead, the material used for manufacturing the plates is reported as rigid PVC (*polyvinyl chloride*). As a result, the simulations are carried out using the PVC material which is already in the material library of COMSOL ($\rho_{\text{PVC}} = 1760 \text{ kg/m}^3$).

4.2.1. Comparison with fundamental analytical models

First, the eigen-frequencies of the flexible plate Case VA0 is computed analytically and compared with numerical results. The

Table 4

Parameters defining the validation test cases. Except from the density, they are taken from the study by Toyoda et al. [6] who reports the sample material as PVC. The density value is taken from the material library of COMSOL.

	Case VA0	Case VA1	Case VA2	Case VA3
d_p [mm]	N/A	0.5	1.0	2.0
t_p [mm]	0.5	0.5	0.5	0.5
b [mm]	N/A	10	10	10
n_p	0	76	76	76
ϕ [%]	0	0.2	0.8	3.0
D [mm]	100	100	100	100
L [mm]	300	300	300	300
L_c [mm]	50	50	50	50
E [N/m ²]	3×10^9	3×10^9	3×10^9	3×10^9
η [-]	0.03	0.03	0.03	0.03
ν [-]	0.3	0.3	0.3	0.3
ρ [kg/m ³]	1760	1760	1760	1760

theoretical modes of a circular plate whose circumference is clamped is calculated by [25]

$$J_0(\gamma_m)I_1(\gamma_m) + I_0(\gamma_m)J_1(\gamma_m) = 0, \quad (15)$$

where subscript m denotes the m th natural mode and

$$\gamma_m = \frac{D}{2} \sqrt{2\pi f_m \left(\frac{\rho_p t_p}{D_p} \right)^{0.5}}. \quad (16)$$

Hence, the eigen-frequencies of a circular plate whose circumference is clamped is found by solving for γ_m in Eq. (16). The first four solutions of this equation and corresponding vacuum eigen-frequencies are given in Table 5.

The eigen-frequencies calculated with the simple analytical approach are compared with the simulation results in Fig. 10. It is seen that the first eigen-frequency in the simulation is significantly larger compared to the analytical calculations. This is due to the additional stiffness added by the air volume in the back cavity. This is verified by carrying out another simulation where the back cavity wall is modelled as a sound-soft boundary, *i.e.* $\hat{p}_2|_{z=L_c} = 0$. Doing so it is ensured that the air in the back cavity can flow through the back and forth through this sound soft boundary and does not exert an additional stiffness on the plate. In other words, by changing the boundary condition, the vacuum

Table 5

The first four vacuum eigen-frequencies of the circular plate whose circumference is clamped. The plate properties are given in Table 4 for a non-perforated plate in vacuum.

γ_m [-]	$\Re\{f_m\}$ [Hz]
3.1962	129
6.3064	500
9.4395	1121
12.5771	1990

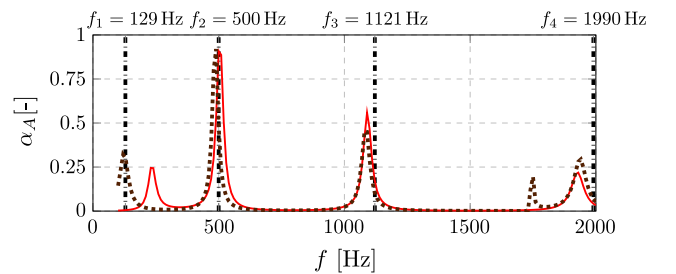


Fig. 10. The comparison between a simple circular plate and the simulations of Case VA0: (•••••) Theoretical eigen-frequencies, (—) simulation with vibro-acoustic coupling, and (---) simulation with vibration only.

Table 6

Corresponding Helmholtz frequency of Cases VA1, VA2 and VA3 (see Table 4).

Simulation case	f_H [Hz]
VA1	420
VA2	682
VA3	1051

modes of the plate described in case VA0 is simulated. The results of this updated simulation validate that the structural properties of the plate is captured successfully in the simulations.

The second basic model is the Helmholtz resonator. The eigen-frequency of a Helmholtz resonator can be calculated by [26]

$$f_H = \frac{c_0}{2\pi} \sqrt{\frac{S_n n_p}{V_0 L_{eq}}}, \quad (17)$$

where $S_n = d_p^2 \pi / 4$ is the cross-section of the perforation, V_0 is the volume of the backing cavity and $L_{eq} = t_p + 1.70(S_n / \pi)^2$ is the equivalent orifice length. In Table 6, the corresponding Helmholtz frequencies of the simulation cases are given.

The calculated Helmholtz frequency values using the analytical expression given in Eq. (17) is marked in the absorption coefficient vs. frequency graphs for Cases VA1, VA2 and VA3 in Fig. 11.

First point to observe in Figs. 10 and 11 is that the absorption peaks originating from structural vibrations are *sharper* and have a more narrow-band character. On the other hand, the peaks related to the acoustic modes are effective over a wide frequency band. This is due to the difference in damping mechanisms between the structural and acoustic systems. Since the acoustic system benefits from the viscous damping, which dissipates more energy in case of high particle velocity, the absorption caused by the air particles passing through the perforations expands over a wider frequency bandwidth.

The key observation from Fig. 11 is that all of the calculated Helmholtz frequencies (see Table 6) are higher than the smooth and wide-band peaks in the absorption curves, which originate

from the acoustic modes of the back cavity and viscous friction in the vicinity of the perforations. This systematic shift to the lower frequencies result from the added mass of the flexible plate described by Cremer [27]. Unlike cases with rigid ones, in non-rigid cavities the compressed air not only pushes out the particles through the perforation, but exerts pressure on the flexible plate also. Therefore, the eigen-frequency corresponding to the fundamental acoustic mode of a non-rigid cavity is referred as *the first cavity resonance frequency*.

4.2.2. Comparison with experimental results

The validation of the discrete numerical model is completed by comparing the predicted absorption coefficient for all cases given in Table 4 with the measurements provided by Toyoda et al. [6] in Fig. 12.

As shown in Fig. 12, the discrete numerical model represents the general behaviour of a vibro-acoustic system successfully. Although, there is a shift between the numerical simulation and experiment results due to the difference in the material properties. When the density is adjusted as a fit parameter to the value $\rho_{PVC} = 1300 \text{ kg/m}^3$, the shift between the numerical simulations and the measurements performed by Toyoda et al. [6] is significantly reduced.

5. Effect of perforation distribution

Three simulation cases illustrate the applicability of the proposed discrete FE model. The effect of perforation distribution is investigated by comparing 3 cases, whose geometric representations are provided in Fig. 13.

For all the cases shown in Fig. 13, the parameters D, L_c, L, E, η, ν and ρ have the same values as in Table 4. Moreover, the parameters $d_p = 1 \text{ mm}, t_p = 0.2 \text{ mm}$ are the same for cases Dist-0, Dist-1 and Dist-2. Table 7 provides the information for the remaining parameters which vary between the test cases and the simulation results are presented in Fig. 14.

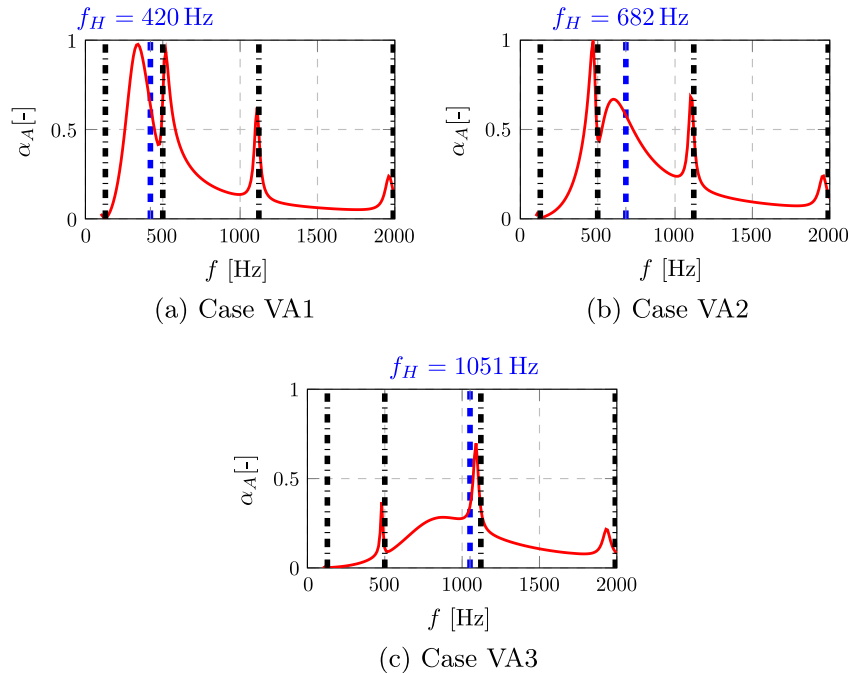


Fig. 11. Cases VA1 (a), VA2 (b), and VA3 (c). The corresponding Helmholtz frequencies are marked on top of the graphs (■-■). Additionally, the first three vacuum eigen-frequencies of the plate are also shown on the graphs (■-■).

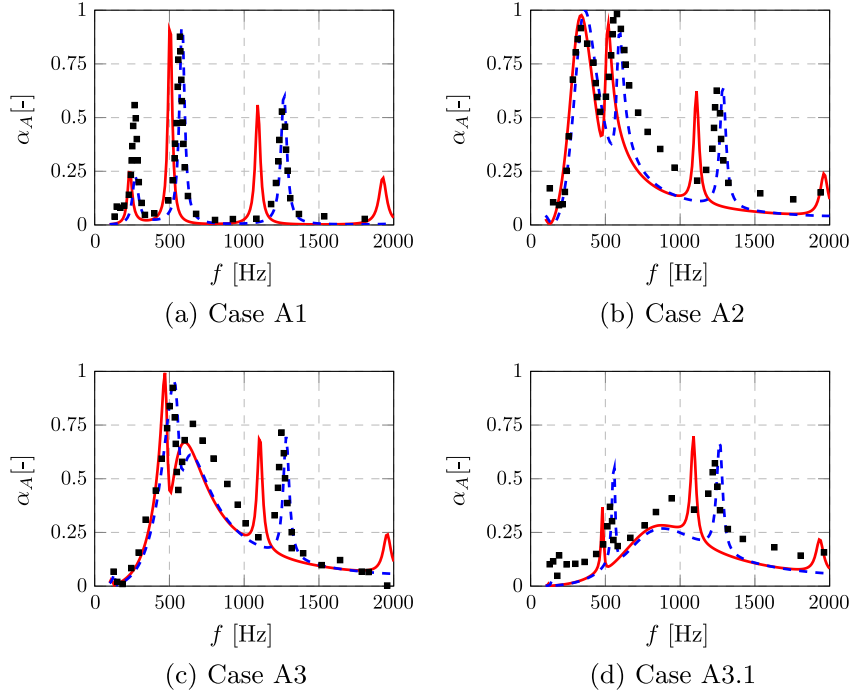


Fig. 12. Comparison between the discrete numerical model (—) and measurements by Toyoda et al. [6] (■). Additional simulations with the density as fit parameter adjusted to $\rho_{PVC} = 1300 \text{ kg/m}^3$ instead of the density reported in the COMSOL library $\rho_{PVC} = 1760 \text{ kg/m}^3$ are shown as (- - -).

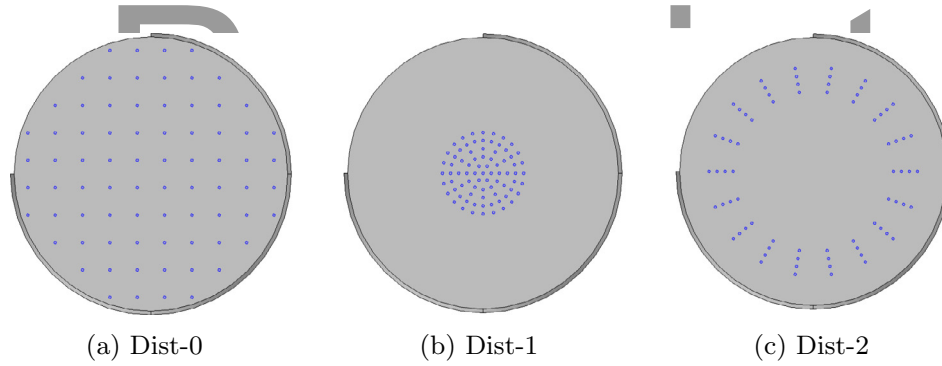


Fig. 13. Models for investigating the effect of perforation distribution: (a) uniform, (b) centered, and (c) peripheral distributions are shown.

Table 7
Parameters varying between test cases Dist-0, Dist-1 and Dist-2.

	Dist-0	Dist-1	Dist-2
n_p	76	79	72
ϕ [%]	0.07	0.07	0.06
b [mm]	10	3	3

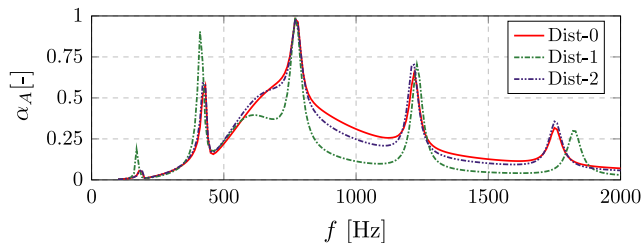


Fig. 14. Effect of perforation distribution. Dist-0: uniform, Dist-1: central, and Dist-2 peripheral distribution (See Fig. 13).

The perforations distributions in Dist-1 and Dist-2 are selected considering the 1st mode of a circular plate which is at its periphery. For this mode, the largest displacement is expected at the center of the plate. Therefore a significant difference is observed for Dist-1 compared to the uniform case (Dist-0). Since the perforations are accumulated at the center, they change the structural properties of the plate locally there. This results with frequency shifts and higher absorption peaks related to the structural vibrations. On the other hand, the sound absorption due to viscous effects deteriorates, which can be an indication of the decrease in the relative velocity between the plate and the air particles. In other words, the plate and the air particles move in phase.

Since the edges are fixed, the local plate velocity is significantly low near the periphery compared to its center. Therefore between the absorption curves of Dist-0 and Dist-2, there is only a slight deviation.

6. Conclusions

A new, efficient numerical model for estimating the absorption characteristics of flexible micro-perforated plates (f-MPPs) is

presented. The model couples the linear acoustics with the shell plate theory. Specifically, the flexible plate is assumed as a shell domain and the micro-perforations are defined separately as imposed transfer impedance boundaries on this domain. The calculation of the transfer impedance value of a single perforation is performed by relations provided by Temiz et al. [16].

Since each perforation is represented separately, the proposed model is referred to as the *discrete* numerical model. During the model building it is observed that the Helmholtz solver takes the area changes into account, hence inserting additional reactance to the modelled system. This additional reactance is calculated for several porosity values and a correction to the transfer impedance expression proposed as a part of the numerical model.

The validation of the discrete numerical model is performed by comparing it to the experiment results. The experiment results from Toyoda et al. [6] is used for validating the vibro-acoustic coupling of the discrete numerical model. Good agreement is achieved between the experimental and numerical results.

The proposed method enables one to treat perforation position as an additional variable. As a result, the effect of non-uniform perforation distribution can be investigated for design purposes. Moreover, even though only circular f-MPPs are studied in this paper, it is possible to use the same model for all types of plate geometries. The model has been used here with impedance of perforations with square edges. The effect of modified edge geometry can be taken into account as proposed by Temiz et al. [16].

The use of the proposed model has been illustrated by an example in a study of the effect of a non-uniform perforation distribution on f-MPPs on the sound absorption. It is observed that the

perforation distribution can have a significant effect on the viscous damping mechanism.

Acknowledgements

The presented work is part of the Marie Curie Initial Training Network Thermoacoustic and Aeroacoustic Nonlinearities in Green combustors with Orifice structures (TANGO). We gratefully acknowledge the financial support from the European Commission under call FP7-PEOPLE-ITN-2012. Thanks to Paula Martínez-Lera for valuable discussions in the process of building the numerical model.

Appendix A. Mesh convergence

A mesh convergence study is performed for the discrete numerical model. Since the most critical part of the numerical domain is around the perforations, the element size representing the perforations is the main focus of this study. The size of the elements in and around one of the perforations is compared in Fig. 15: Mesh-1 is the typical mesh built for the simulations in this study and Mesh-2 is the finer mesh built for checking the effect of element size.

The parameters of the numerical model used for comparing the effect of mesh is chosen among the test cases, *i.e.* VA1 (see Table 4). The reason for selecting this particular case is that it has the smallest perforation diameter, thus the number of elements in perforations is more critical than other cases in this study.

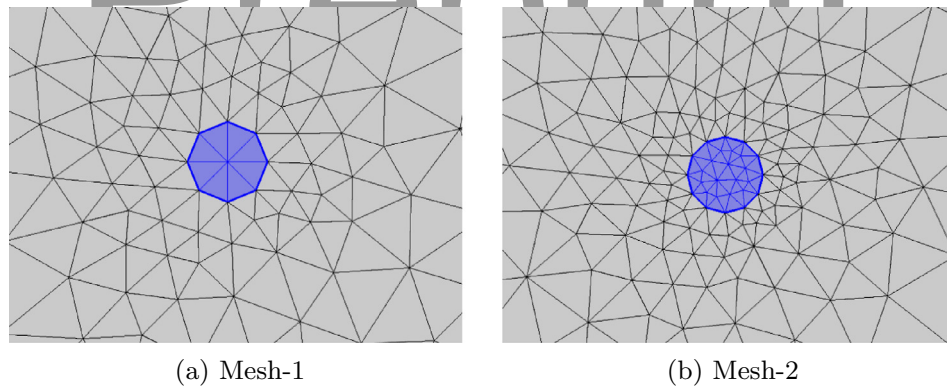


Fig. 15. The element size comparison for two meshes built to represent the same geometry. The diameter of the perforation here is 0.5 mm.

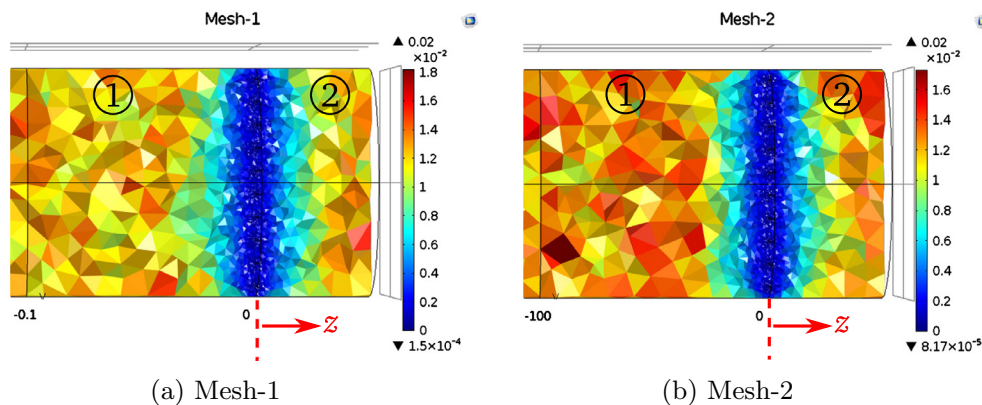


Fig. 16. A slice of the numerical domain in yz -plane to show the gradual increase of the element size from the plate to the rest of the acoustic domain. Different colours represent the element size and the dimensions provided in the scale are in [m].

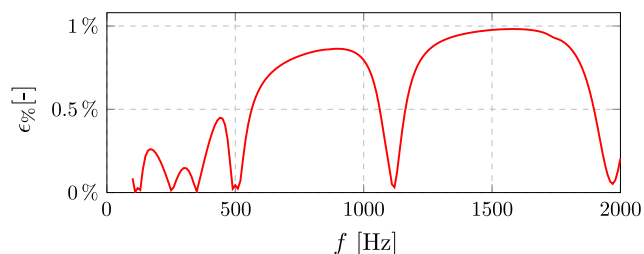


Fig. 17. The relative percentage error between Mesh-1 and Mesh-2. Increasing the number of elements in the perforation by 5 times in each perforation results in a difference of less than 1% relative error in the absorption coefficient. Please note that when the absorption coefficient is not close to zero, the relative error is even less.

To minimize the number of elements in the mesh, a gradually increasing element size is used. The maximum growth rate of the elements are selected as 1.35 in this study. As a result, once the size of the elements around the perforations become smaller, they affect the size of the elements around. The gradual change in the element size away from the plate is given for Mesh-1 and Mesh-2 in Fig. 16.

In Figs. 15 and 16, it is seen that Mesh-2 has 5 times more elements in a perforation compared to Mesh-1. Moreover, the size of the elements are decreased both for the plate and the acoustic volume around the perforation. In general, the number of elements in Mesh-2 is 30% more than those of Mesh-1. To assess this effect on the absorption coefficient, the relative percentage error, $\epsilon_{\%}$, is calculated as follows:

$$\epsilon_{\%} = \frac{|\alpha_{A_2} - \alpha_{A_1}|}{\alpha_{A_2}} 100\%, \quad (18)$$

where α_{A_1} and α_{A_2} are the absorption coefficients calculated in the simulations using Mesh-1 and Mesh-2, respectively. The graph over the frequency range of interest, $100 \text{ Hz} \leq f \leq 2000 \text{ Hz}$ is illustrated in Fig. 17.

In Fig. 17, it is seen that, increasing the number of elements in the perforations by factor 5 does not affect the absorption coefficient more than 1% for $100 \text{ Hz} \leq f \leq 2000 \text{ Hz}$. Considering the absorption coefficient vs. frequency graph of Case VA1 (see Fig. 12), the increase in $\epsilon_{\%}$ is due to the evaluation of the ratio of two small numbers. For absorption peaks, the relative percentage error is significantly lower than 1%.

References

- [1] Maa D-Y. Potential of microperforated panel absorber. *J Acoust Soc Am* 1998;104(5):2861–6.
- [2] Cremer L, Müller HA. Principles and applications of room acoustics, vol. 2. London: Applied Science Publishers; 1978. translated by T.J. Schultz in 1982.
- [3] Basten TGH, van der Hoogt PJM, Spiering RMEJ, Tijdeman H. On the acousto-elastic behaviour of double-wall panels with a viscothermal air layer. *J Sound Vib* 2001;243(4):699–719.
- [4] Lee J, Swenson GW. Compact sound absorbers for low frequencies. *Noise Control Eng J* 1992;38(3):109–17.
- [5] Lee YY, Lee EWM, Ng CF. Sound absorption of a finite flexible micro-perforated panel backed by an air-cavity. *J Sound Vib* 2005;287:227–43.
- [6] Toyoda M, Mu RL, Takahashi D. Relationship between Helmholtz-resonance absorption and panel-type absorption in finite flexible microperforated-panel absorbers. *Appl Acoust* 2010;71(4):315–20.
- [7] Bravo T, Mauri C, Pinhède D. Sound absorption and transmission through flexible micro-perforated panels backed by an air layer and a thin plate. *J Acoust Soc Am* 2012;131(5):3853–63.
- [8] Bravo T, Mauri C, Pinhède D. Enhancing sound absorption and transmission through flexible multi-layer micro-perforated structures. *J Acoust Soc Am* 2013;134(5):3663–73.
- [9] Li C, Cazzolato B, Zander A. Acoustic impedance of micro perforated membranes: velocity continuity condition at the perforation boundary. *J Acoust Soc Am* 2016;139(1):93–103.
- [10] Hou K, Bolton JS. Finite element models for micro-perforated panels. In: Proceedings of inter-noise 2009, Ottawa, Canada; 2009. no. 499.
- [11] Wang C, Huang L. On the acoustic properties of parallel arrangement of multiple micro-perforated panel absorbers with different cavity depths. *J Acoust Soc Am* 2011;130(1):208–18.
- [12] Okuzono T, Sakagami K. A finite-element formulation for room acoustics simulation with microperforated panel sound absorbing structures: verification with electro-acoustical equivalent circuit theory and wave theory. *Appl Acoust* 2015;95:20–6.
- [13] Carbajo J, Ramis J, Godinho L, Amado-Mendes P, Alba J. A finite element model of perforated panel absorbers including viscothermal effects. *Appl Acoust* 2015;90:1–8.
- [14] Kinsler LE, Frey AR, Coppens AB, Sanders JV. Fundamentals of acoustics. 4th ed. New York: John Wiley and Sons; 2000.
- [15] Kirchhoff G. Über das Gleichgewicht und die Bewegung einer elastischen Scheibe. *J die Reine Angew Math* 1850;40:51–88.
- [16] Temiz MA, Lopez Arteaga I, Efraimsson G, Åbom M, Hirschberg A. The influence of edge geometry on end-correction coefficients in micro-perforated plates. *J Acoust Soc Am* 2015;138(6):3668–77.
- [17] COMSOL Inc., COMSOL multiphysics; 2015. <<https://www.comsol.com>> [accessed 19-October-2016].
- [18] Temiz MA, Tournadre J, Lopez Arteaga I, Martinez-Lera P, Hirschberg A. Numerical estimation of the absorption coefficient of flexible micro-perforated plates in an impedance tube. In: 23rd International congress on sound and vibration (ICSV 2016), Athens; 2016.
- [19] Bodén H, Åbom M. Influence of errors on the two-microphone method for measuring acoustic properties in ducts. *J Acoust Soc Am* 1986;79:541–9.
- [20] Siemens PML Software, LMS Virtual.Lab 13.1; 2014. <https://www.plm.automation.siemens.com/en_us/products/lms/virtual-lab/> [accessed 19-October-2016].
- [21] Ingard U. On the theory and design of acoustic resonators. *J Acoust Soc Am* 1953;25(6):1037–61.
- [22] Pierce AD. Acoustics: an introduction to its physical principles and applications. In: [28]; 1989. p. 339–41 [chapter 7].
- [23] Tayong R, Dupont T, Leclaire P. Experimental investigation of holes interaction effect on the sound absorption coefficient of micro-perforated panels under high and medium sound levels. *Appl Acoust* 2011;72(10):777–84.
- [24] Temiz MA, Lopez Arteaga I, Efraimsson G, Åbom M, Hirschberg A. Acoustic end correction in micro-perforated plates – revisited. In: 21st International congress on sound and vibration 2014 (ICSV 2014), vol. 2, Beijing; 2014. p. 1203–9.
- [25] Kelly P. Solid mechanics Part II: Engineering solid mechanics. <http://homepages.engineering.auckland.ac.nz/pkel015/SolidMechanicsBooks/Part_II/index.html> [accessed: 2016-08-21].
- [26] Pierce AD. Acoustics: an introduction to its physical principles and applications. In: [28]; 1989. p. 330–3 [chapter 7].
- [27] Cremer L. The physics of the violin. Massachusetts: The MIT Press; 1981. translated by J.S. Allen in 1984.
- [28] Pierce AD. Acoustics: an introduction to its physical principles and applications. 2nd ed. New York: McGraw-Hill; 1989.